

Magnetically Driven Accretion in the Kerr Metric III: Unbound Outflows

Jean-Pierre De Villiers¹, John F. Hawley

*Astronomy Department
University of Virginia
P.O. Box 3818, University Station
Charlottesville, VA 22903-0818*

and

Julian H. Krolik, Shigenobu Hirose
*Physics and Astronomy Department
Johns Hopkins University
Baltimore, MD 21218*

vjpde@ucalgary.ca; jh8h@virginia.edu; jhk@pha.jhu.edu; shirose@pha.jhu.edu

ABSTRACT

We have carried out fully relativistic numerical simulations of accretion disks in the Kerr metric. In this paper we focus on the unbound outflows that emerge self-consistently from the accretion flow. These outflows are found in the axial funnel region and consist of two components: a hot, fast, tenuous outflow in the axial funnel proper, and a colder, slower, denser jet along the funnel wall. Although a rotating black hole is not required to produce these unbound outflows, their strength is enhanced by black hole spin. The funnel-wall jet is excluded from the axial funnel due to elevated angular momentum, and is also pressure-confined by a magnetized corona. The tenuous funnel outflow accounts for a significant fraction of the energy transported to large distances in the higher-spin simulations. We compare the outflows observed in our simulations with those seen in other simulations.

Subject headings: Black holes - magnetohydrodynamics - jets - stars:accretion

¹Now at Dept. of Physics and Astronomy, University of Calgary, 2500 University Drive NW, Calgary, Alberta, T2N 1N4

1. Introduction

Over thirty years ago jets entered the lexicon of astrophysical phenomena when it was realized that the double radio sources observed in some galaxies are the product of tightly collimated bidirectional outflows. Since then there has been substantial progress in both jet theory and jet observations. We now know that in addition to active galaxies, jets are found in mass-transfer binaries, galactic microquasars, protostellar systems, and pulsars such as in the Crab nebula. Collimated outflows are clearly a natural occurrence, not solely the result of some rare and unusual circumstance in the core of a few active galaxies.

Much of the theoretical work on jets has concentrated on broad questions of collimation, and properties and stability of the propagating jet itself. A more difficult issue seems to be how the jet is formed in the first place. While a variety of radiative and hydrodynamic processes have been examined as possible jet launch mechanisms, the consensus that has emerged is that jets are fundamentally a magnetohydrodynamic (MHD) phenomenon, most often associated with an accretion disk (as argued, for example, by Livio 2002). This picture is further supported by the knowledge that accretion disks are themselves fundamentally MHD; accretion is driven by MHD turbulence resulting from the magnetorotational instability (MRI; Balbus & Hawley 1998).

No other known mechanism works as well and as naturally as large-scale magnetic fields to both accelerate and collimate an outflow. Stresses in large-scale poloidal fields that thread through the disk at the appropriate angles can accelerate plasma directly into a strong outflow. This magneto-centrifugal acceleration is sometimes referred to as the Blandford-Payne mechanism, after the influential paper of Blandford & Payne (1982). Strong magnetic pressure gradients resulting from amplified toroidal fields have also been proposed as an acceleration mechanism. Regardless of the mechanism that drives the initial acceleration, a large-scale poloidal field or a strong toroidal field can provide effective collimation of the resulting outflow.

In these scenarios the energy for the jet comes from the disk and the accretion therein. The rotation of the central compact object, however, is also a source of energy, even if the central object is a black hole. The Blandford & Znajek (1977) mechanism, for example, envisions field lines connected directly to a rotating black hole; the rotation drives outward-going Alfvén waves. Punsly & Coroniti (1990) suggested an indirect magnetohydrodynamic mechanism for accomplishing much the same end, by having the fields anchored in plasma orbiting near the rotating black hole. In either case, some of the black hole’s spin energy is extracted and transported outward as a Poynting flux.

Numerical simulations have long played an important role in examining and validating

many aspects of jet physics. The work of Shibata & Uchida (1985) provides one of the earliest examples. They simulated an accreting disk of rotating gas, transfixing by vertical magnetic field. In this simulation radial field formed in the disk by infall is twisted into strong toroidal field, which provides strong vertical magnetic pressure forces to drive an outflow that is collimated along the vertical field. Since this pioneering effort, many simulations have been performed, featuring improved resolution, additional physical mechanisms, longer time evolution, larger spatial domains, and even full three dimensions. However, most of these jet simulations have, like Shibata & Uchida, featured a large-scale poloidal magnetic field as part of the initial conditions. In some cases a further simplification has been made by treating the underlying accretion disk as a boundary condition. In such studies the focus is on the ability of this large-scale field to accelerate and collimate gas supplied by the disk boundary (e.g., Meier *et al.* 1997; Romanova *et al.* 1997, Ouyed & Pudritz 1997; Krasnopolsky, Li, & Blandford 1999). Details differ from simulation to simulation, in such things as the assumed magnetic field and the properties of the disk boundary conditions, but, taken as a whole, the results provide strong overall support for the magnetic launch and collimation scenario.

There remain, however, several significant questions that cannot be answered by simulations of this sort. First, do jets always require a net large-scale poloidal field? Under what circumstances do such fields develop? Can they be generated by a dynamo operating within the disk, or must net field be brought in from large radius and concentrated near the center? These questions must be addressed with fully global accretion simulations that do not assume the presence of a large-scale field as an initial condition.

In contrast to simulations that have focused on jets, the simulations developed for this series of papers has been directed toward the dynamical properties of the black hole accretion disk itself. Using a general relativistic MHD (GRMHD) code we have investigated accretion disk structures that form from an initial condition consisting of an isolated torus of gas fully enclosing a weak initial magnetic field. An advantage of such an initial condition is that it is independent of the boundary conditions. Rather than assuming a pre-existing large-scale field configuration, we can study the circumstances under which such large-scale fields might develop naturally in the accretion flow.

The first paper of this series, De Villiers, Hawley, & Krolik (2003; hereafter Paper I) presented an overview of a series of 3D general relativistic MHD simulations of Keplerian accretion disks orbiting Kerr black holes (the “KD” simulations). The second paper of the series (Hirose *et al.* 2004; hereafter Paper II) discussed the overall magnetic field configurations in the accretion flow. Among the results noted in Paper I was the appearance of funnel-wall jets in all simulations. Such jets were also observed in a previous simulation using a pseudo-Newtonian potential rather than full GR (Hawley & Balbus 2002; hereafter

HB02). Kato *et al.* (2004) have also carried out similar pseudo-Newtonian simulations and analyzed in greater detail the jets that were produced. More recently, jets were noted in 2D axisymmetric GR simulations by McKinney & Gammie (2004). What is noteworthy in all these simulations is the natural emergence of jets from accretion disks that did not have large-scale fields included as an initial condition. These results have the potential to greatly improve our understanding of the link between accretion and large scale outflows, since these jets arise *self-consistently* from the accretion process. The success—or failure—of any self-consistent simulation to produce jets will help to define the range of circumstances that determine jet production in astrophysical systems.

In this paper, we will focus on the properties of the funnel-wall jets seen in the KD simulations. Relevant background material from Paper I is briefly outlined in §2. In §3 we analyze the unbound outflows seen in the KD simulations. We include an overview of the jets, and the details of separate regions within the jets. In §4 we briefly review the jets seen in other accretion simulations. In §5 we provide a summary of these results.

2. Overview of Simulations

We solve the equations of ideal MHD in the metric of a rotating black hole. The specific form of the equations we solve, and the numerical algorithm incorporated into the GRMHD code are described in detail in De Villiers & Hawley (2003; hereafter DH03a). For reference we reiterate here the key terms and the definitions of the primary code variables.

We work in the Kerr metric, expressed in Boyer-Lindquist coordinates, (t, r, θ, ϕ) , for which the line element has the form, $ds^2 = g_{tt} dt^2 + 2g_{t\phi} dt d\phi + g_{rr} dr^2 + g_{\theta\theta} d\theta^2 + g_{\phi\phi} d\phi^2$. We use the metric signature $(-, +, +, +)$. The determinant of the 4-metric is g , and $\sqrt{-g} = \alpha \sqrt{\gamma}$, where α is the lapse function, $\alpha = 1/\sqrt{-g^{tt}}$, and γ is the determinant of the spatial 3-metric. We follow the usual convention of using Greek characters to denote full space-time indices and Roman characters for purely spatial indices. We use geometrodynamical units where $G = c = 1$; time and distance are in units of the black hole mass, M .

The state of the relativistic test fluid at each point in the spacetime is described by its density, ρ , specific internal energy, ϵ , 4-velocity, U^μ , and isotropic pressure, P . The relativistic enthalpy is $h = 1 + \epsilon + P/\rho$. The pressure is related to ρ and ϵ through the equation of state of an ideal gas, $P = \rho\epsilon(\Gamma - 1)$, where Γ is the adiabatic exponent. For these simulations we take $\Gamma = 5/3$, unless otherwise indicated. The magnetic field of the fluid is described by two sets of variables, the constrained transport magnetic field, $F_{jk} = [ijk] \mathcal{B}^i$, and magnetic field 4-vector $\sqrt{4\pi} b^\mu = {}^*F^{\mu\nu} U_\nu$. The ideal MHD condition requires

$U^\nu F_{\mu\nu} = 0$. The magnetic field b^μ is included in the definition of the total four momentum, $S_\mu = (\rho h + \|b\|^2) W U_\mu$, where W is the Lorentz factor. We define auxiliary density and energy functions $D = \rho W$ and $E = D \epsilon$, and transport velocity $V^i = U^i/U^t$. We also define the specific angular momentum as $l = -U_\phi/U_t$ and the angular velocity as $\Omega = U^\phi/U^t$.

In Paper I, we presented results of a series of high- and low-resolution simulations, the KD (Keplerian Disk) set of disk models. These models have an initial condition consisting of an isolated gas torus orbiting near the black hole, with a pressure maximum at $r \approx 25M$, and a slightly sub-Keplerian initial distribution of angular momentum throughout. The initial magnetic field consists of loops of weak poloidal field lying along isodensity surfaces within the torus. The emphasis in this paper will be on the high-resolution models designated KD0, KDI, KDP, and KDE. These differ in the spin of the black hole around which they orbit, with $a/M = 0, 0.5, 0.9$ and 0.998 respectively. These models used $192 \times 192 \times 64$ (r, θ, ϕ) grid zones. The radial grid is set using a hyperbolic cosine function to maximize the resolution near the inner boundary. The inner boundary is at $r_{in} = 2.05 M, 1.90 M, 1.45 M,$ and $1.175 M$ for models KD0, KDI, KDP, and KDE, respectively, and the outer radial boundary is set to $r_{out} = 120M$ in all cases. The θ -grid ranges over $0.045\pi \leq \theta \leq 0.955\pi$, with an exponential grid spacing function that concentrates zones near the equator; reflecting boundary conditions are enforced in the θ -direction. The ϕ -grid spans the quarter plane, $0 \leq \phi \leq \pi/2$.

Although we will focus our analysis on the KD models, we also will draw upon the results of a number of other models for comparison purposes. Most of these other models are run at lower resolution, using $128 \times 128 \times 32$ grid zones. The effects of numerical resolution will be gauged in part by a direct comparison between KDP and the lower-resolution model KDP_{lr} (Paper I). We will examine the series of models that began with constant angular momentum tori around holes with $a/M = -0.998, 0.0,$ and 0.9 , the ‘‘SF’’ models described in De Villiers & Hawley (2003; hereafter DH03b). We will also consider the presence (or absence) of jets in several pseudo-Newtonian simulations. Finally we will present some results from two new simulations, a high-resolution simulation with $\Gamma = 4/3$, and a disk with an initial toroidal field.

2.1. Simulation diagnostics

Three-dimensional numerical simulations generate an enormous amount of data, only a representative sample of which can be examined. Our analysis is based on a specific set of volume- and shell-averaged history data, taken every M in time, and complete data snapshots taken every $80M$ in time. In addition, the complete density field is output every

$2M$ for use in making highly time-resolved animations. Although the details of the history calculations are given in Paper I, we provide here a brief summary to clarify the calculations of mass, energy, and angular momentum transported by the unbound outflows. The flux \mathcal{F} of a given quantity through a shell at radius r is computed using

$$\langle \mathcal{F} \rangle(r) = \int \int \mathcal{F} \sqrt{-g} d\theta d\phi, \quad (1)$$

where the bounds of integration range over the full θ and ϕ computational domains. We evaluate the rest mass flux $\langle \rho U^r \rangle$, energy flux $\langle T^r_t \rangle$ and the angular momentum flux $\langle T^r_\phi \rangle$. Since we are interested in material that leaves the computational domain through the outer boundary, we will refer to these fluxes as ejection rates when they are evaluated at the outer boundary, r_{out} . Gas that leaves the grid at the inner radial boundary is considered to be accreted into the black hole; we refer to this as the black hole accretion rate. We account for changes in the total mass, energy, and angular momentum in terms of the corresponding net fluxes that leave the grid, either into the hole or out of the grid, by integrating over time,

$$\{\mathcal{F}\}_{out} = \int dt \langle \mathcal{F} \rangle(r_{out}), \quad (2)$$

for example.

The data on radial fluxes found in the time-history data is insufficient for the present study. For example, not all of the gas leaving the grid at the outer boundary is unbound; to distinguish between bound and unbound matter, we impose on the integrands the restriction that the specific total energy satisfy $-h U_t > 1$ when seeking to include only unbound material. This can be computed only by using the complete data dumps made every $80M$ in time.

One of the important issues in jet physics is the nature of the forces that account for jet acceleration. To compute forces from the simulation data, we begin with the conservation law $\nabla_\mu T^{\mu\nu} = 0$, where the energy-momentum tensor consists of a fluid part, $T_{(FL)}^{\mu\nu} = \rho h U^\mu U^\nu + P g^{\mu\nu}$, and an electromagnetic part, $T_{(EM)}^{\mu\nu} = (4\pi)^{-1} (F^\mu_\alpha F^{\nu\alpha} - F_{\alpha\beta} F^{\alpha\beta} g^{\mu\nu}/4)$. As described in DH03a, the momentum equation used in the numerical solver is obtained by applying the projection tensor, $h_{\alpha\nu} = g_{\alpha\nu} + U_\alpha U_\nu$, to the conservation law. Doing this, and then using the equations for conservation of energy ($U_\nu \nabla_\mu T^{\mu\nu} = 0$) and baryon number ($\nabla_\mu \rho U^\mu = 0$), it is straightforward to show that the fluid portion of the momentum equation can be rewritten as

$$h_{\alpha\nu} \nabla_\mu T_{(FL)}^{\mu\nu} = \rho h U^\mu \nabla_\mu U_\alpha + (\nabla_\alpha P + U_\alpha U^\nu \nabla_\mu P) \quad (3)$$

One can express the divergence of the electromagnetic part of the energy-momentum tensor in terms of the Lorentz force, $\nabla_\mu T_{(EM)}^{\mu\nu} = -J_\mu F^{\mu\nu}$ (Misner, Thorne, & Wheeler, 1973;

hereafter MTW), where J^μ is the current 4-vector, $J^\mu = (4\pi)^{-1} \nabla_\nu F^{\nu\mu}$. Applying the projection tensor to this result, along with the ideal MHD condition, $U_\mu F^{\mu\nu} = 0$, and grouping with the previous result, we obtain the force law,

$$\rho h U^\mu \nabla_\mu U_\alpha = -(\nabla_\alpha P + U_\alpha U^\nu \nabla_\nu P) + J_\mu F^\mu{}_\alpha, \quad (4)$$

where the left-hand side represents the product of inertia and 4-acceleration acting on the fluid, and the right-hand side represents the sum of the pressure-gradient and Lorentz forces acting on the fluid. As pointed out in MTW, this is a very useful form of the momentum equation, since the right-hand side expresses departure from geodesic motion (i.e., the right-hand side is identically zero for free-falling dust). However, in the present context this formulation has the disadvantage that the centrifugal and Coriolis force terms are hidden in the left hand side. Similarly, the “J dot F” term combines contributions from both magnetic pressure gradients and Maxwell stresses; in order to distinguish between these two contributions, it is possible to evaluate the components of $\nabla_\mu T_{(EM)}^{\mu\nu}$ using the secondary code variables for the magnetic field, b^μ .

The contribution due to pressure gradients can be expressed as a 4-vector

$$\mathcal{F}_{(P)}^\mu = -(g^{\mu\nu} \nabla_\nu P + U^\mu U^\nu \nabla_\nu P) = -h^{\mu\nu} \nabla_\nu P, \quad (5)$$

an expression which can be readily evaluated using code variables. We can similarly write an expression for the Lorentz force 4-vector,

$$\mathcal{F}_{(L)}^\mu = h^{\mu\nu} J^\alpha F_{\alpha\nu}. \quad (6)$$

Recall that $F_{\alpha\nu}$ are the CT magnetic field and EMFs [eqns.(14) and (35) of DH03a], which are the fundamental magnetic field variables evolved in the code. Evaluation of J^α requires data for three adjacent time steps, since time derivatives must be evaluated. Such datasets were generated from the late-time data dumps by direct evolution using the GRMHD code.

3. Unbound outflows in KD models

The unbound outflow is, at its most basic level, that portion of the flow that is *outbound* and *unbound*. Specifically, it is where the radial momentum is positive, and the specific energy at infinity is greater than unity, i.e. $-hU_t > 1$. These criteria are met in the axial funnel and the funnel wall regions of the simulation volume, and the unbound outflow can be divided into two sub-regions: a hot, tenuous, fast component in the funnel, and a colder, denser, slower component along the funnel wall. These two regions have distinctive properties. We turn to the dense funnel-wall component first.

The basic structure of the funnel-wall component is illustrated by Figure 1, which consists of still frames taken from an animation of gas density ρ_{jet} , that is the density ρ where $-hU_t > 1$, for model KDP (which most clearly exhibits the jet properties observed in the KD models). The animation frames show that the unbound density forms a biconical outflow lying along a narrow boundary between the largely evacuated axial funnel and the coronal envelope, hence the name “funnel-wall jet” introduced in Paper I.

The funnel-wall jets are not transient features in these models. They are established early in the simulation at a time coincident with the establishment of the quasi-steady accretion flow into the black hole, and they endure for the length of the simulation. We have compiled extended animation sequences of the jets, and Figure 1 presents two views at two different times from such a sequence, one view looking onto the jet from the funnel side of the computational volume and the other from the corona side. The quarter hourglass shape corresponds to the coordinate range in ϕ used in the simulation. The complete animation sequence reveals that the funnel-wall jet is highly dynamical, and its shape varies on a time scale comparable to the orbital period of the main disk body. This variability is due in part to a changing dynamical balance between forces in the magnetically-dominated funnel and the coronal envelope, as well as variations in the rate at which matter is injected into the jet. The variable injection rate can be seen in the relatively dense spiral features that appear near the base of the jet and propagate outward, becoming more diffuse. Density variations also appear as episodic axisymmetric “rolls” that propagate outward; an example of this is visible halfway up the upper jet in the top panels of the figure. Such rolls appear to be correlated with the arrival of especially dense knots of material in the inner torus region; part of this material is then expelled through the jet in a more or less axisymmetric manner.

In contrast to the funnel-wall jet, the axial funnel component of the unbound outflow is largely invisible in density and mass flux plots. However, as noted in Paper I, the axial funnel contains a tenuous, hot, fast radial outflow with a significant electromagnetic component.

To organize the discussion we divide the unbound outflow into distinct regions, as suggested by the animations and from qualitative analysis. For brevity, we will refer to the dense, cold funnel-wall jet simply as “the jet”, and the hot outflow in the axial funnel as “the funnel outflow”. The various components of the unbound outflow are illustrated in Figure 2, which shows an azimuthally-averaged composite from model KDP. The color contours depict gas density on a logarithmic scale. The boundary of the jet is indicated by a thick white contour; this boundary is set by two conditions. The contour nearest the corona marks the boundary between gas that is bound and gas that is unbound. The contour nearest the funnel indicates where the positive radial mass flux has dropped below a limit we use to define the funnel wall jet, $(\rho U^r)_{jet} \gtrsim 10^{-4}(\rho U^r)_{max}$, where $(\rho U^r)_{max}$ denotes the maximum

unbound outward mass flux. The vector field indicates the direction, but not the magnitude of pressure gradients and Lorentz forces.

The labels in the figure identify the five main regions that we will discuss. These are:

- (1) The **body of the jet** is depicted in Figure 1 and consists of the hourglass-shaped (hollow cone) region where there is significant unbound outward mass flux. Inside the cone is the axial funnel where the density is very low, and outside the cone lies coronal envelope consisting of bound material.
- (2) The **base of the jet** is the origin of the continuous region of unbound, outgoing radial mass flux. In the high-spin KDP the base is relatively stable and is marked by a ring of denser gas. In low-spin models the base is not so sharply defined, instead showing both spatial and temporal variability.
- (3) The **injection region** is where mass is injected into the unbound outflow. This region begins where the inner torus, coronal envelope, and axial funnel converge, at a distance comparable to the marginally stable orbit, r_{ms} . The mass flux in the jet is not uniform, but varies with time and increases with increasing radius.
- (4) The **funnel outflow** consists of a tenuous, fast, unbound outflow. The axial funnel contains a large-scale poloidal magnetic field similar to a split monopole, as discussed in Papers I and II. This field is established during the ejection of low-density magnetized material into the funnel in the early stages of accretion. If the black hole is rotating, this funnel field is wound up and amplified by frame dragging, creating a toroidal field and an outward-going energy flux (e.g., figs. 6 and 7 in Paper II).
- (5) To discuss possible asymptotic properties of the jet, we refer to the **outflow region**, which is the distant region well away from the disk and the black hole where the jet is moving ballistically. We take the outflow region to lie just inside the outer grid boundary which is located at $r = 120M$. Various quantities can be computed here and compared between the different KD models.

In the following subsections, we consider each of these regions in turn.

3.1. The body of the jet

Figure 3 presents a cut through a representative region of the jet body for all four KD models. It depicts four sets of variables as functions of polar angle, θ , from the “North” polar

axis to the equator; the variables are azimuthally-averaged, and taken at a radial distance of $10 r_{ms}$.

The top graph in each panel is the unbound outward mass flux, ρU^r , as defined above. The units are the fraction of the maximum mass flux in the jet. This defines the funnel wall jet, and its angular width is represented by the shaded region which extends to the lower graphs. One can see that the peak flux lies just inside the boundary with the corona, and the flux drops off rapidly toward the funnel. This peak tends to shift more toward the coronal boundary of the jet with increasing black hole spin.

The second graph from the top shows gas density, and the gas and magnetic pressures. Density is normalized to its peak value, which is found at the equator. Gas and magnetic pressure are normalized to the peak *total* pressure, also found at the equator. The density in all models decreases steadily through the corona, and shows a sharp roll-off through the jet. The gas pressure has a similar profile, except that the decrease through the jet is not as pronounced, especially in models KDP and KDE. In the latter case, the gas pressure through the jet and funnel is roughly constant. The gas temperature is quite high in the funnel since the low-density gas has been heated by shocks driven into the funnel from denser regions of the flow. The θ -profile of the magnetic pressure is much more shallow than that of gas pressure in all the models. In model KD0, magnetic pressure is roughly constant through the funnel, dips slightly through the jet and corona, then rises slightly through the body of the disk. In models KDI, KDP, and KDE, magnetic pressure is roughly constant in the funnel and jet, dipping slightly in the corona, near the jet boundary, before rising again as one moves toward the equator. As was pointed out in Paper I (see fig. 8), the total pressure is relatively smooth through the corona into the funnel. The funnel is magnetically dominated, the main disk is gas-pressure dominated, and the corona has a ratio of pressures near unity. The unbound mass outflow is found just inside the region where $\beta = P_{gas}/P_{mag}$ drops below unity.

The third graph from the top shows the fluid and electromagnetic contributions to outward energy flux ($T^r_{t(\text{fluid})}$ and $T^r_{t(\text{EM})}$), normalized to the maximum of the absolute total energy flux, which is found near the equator in all cases. The fluid component varies in sign in the main disk and corona, as would be expected for turbulent motions. Its absolute value shows a steady drop from the main disk body through the corona. In the unbound portions of the outflow, energy flux is everywhere outward. The fluid energy flux is roughly constant within the axial funnel; it is due to high enthalpy and high outflow velocities. The electromagnetic component of the energy flux is extremely weak in model KD0, and becomes more prominent in the funnel with increasing black hole spin.

In the lower graph we plot the absolute value of the magnetic stress, $\|b^r b_\phi\|$, again

normalized to its maximum value on the slice of constant radius. This quantity exhibits a strong dependence on black hole spin in the jet and the funnel. In model KD0, the stress drops sharply in crossing from the main disk body to the corona. Though stress is variable through the corona, the peaks are roughly level. Peak stress in the jet is slightly weaker than in the corona, and extremely weak in the funnel. The models with a rotating hole also show a drop in stress in the corona, relative to the main disk. However, stress in the jet and funnel becomes progressively more dominant with increasing spin, with the maximum stress found inside the funnel in models KDP and KDE. In these three models, stress in the jet drops from the funnel to the corona side, indicating that the stress acting on the jet material is strongest where the density is low.

The fluid velocity also makes a sharp transition through the jet, from predominantly orbital motion in the corona to radial or helical motion in the funnel. As noted in Paper II the magnetic field lines also undergo a corresponding transition through the funnel wall. The outward velocity increases sharply through the funnel wall. The mass-weighted mean of V^r within the funnel wall jet ranges from $\approx 0.3c$ for model KD0 to $0.5c$ for model KDE. The velocity is predominantly radial on the funnel side and toroidal on the corona side of the jet. The values are comparable to the toroidal velocities found in the inner torus which range from $\approx 0.4c$ in KD0 to $0.6c$ in KDE. The outward speed at a fixed angle is established quite close in: the flow accelerates from near its base to $10\text{--}20M$ (the end of the acceleration zone moves outward with decreasing black hole spin) and then retains that speed all the way to the outer boundary at $120M$.

3.2. The base of the jet

We define the base of the jet as the point closest to the black hole where there is a continuous flow of unbound mass to the outer boundary. In general this point varies in time, but model KDP has a base that is compact, largely axisymmetric, and found at a more or less fixed location over extended periods of time, making it ideal for illustration purposes. Figure 5 shows the azimuthally-averaged radial mass flux in KDP in the inner region of the flow. The yellow and red colors indicate outflow, and the circle locates the base. (Note a small disconnected segment of positive flux nearer the black hole, which is not part of the jet.) The jet originates on the surface of the inner torus in the vicinity of r_{ms} ($= 2.32M$ in KDP). In this and all models where jets have been observed, the base of the jet is found where inner torus, coronal envelope, and axial funnel intersect.

Figure 5 also depicts a set of three equipotentials for marginally bound material that bracket the critical contour ($\Phi_{mb} = [-0.01, 0, 0.01]$, where $\Phi_{mb} = \log[-U_t(l_{mb}, a; r, \theta)]$). These

equipotentials are of interest for comparison to constant-angular momentum thick disk models (e.g., Abramowicz et al. 1978). The base of the jet lies above the critical contour ($\Phi_{mb} = 0$), which suggests that the outbound flow of the jet lies up against the centrifugal barrier. The jet appears to be squeezed by the pressure of the inner torus and corona against the centrifugal barrier that defines the funnel. Since material with angular momentum cannot encroach into the funnel, the jet material is compelled to exit along the funnel wall.

The launching of a jet appears to be facilitated by a geometrically thick inner torus deep in the potential well of the black hole. As discussed in Paper I, the inner torus moves closer to the black hole and becomes denser and thicker with increasing black hole spin. This spin-dependent increase in the size of the inner torus provides one indirect way in which black hole spin could increase the mass flux in the jet. Both the jet mass flux and the accretion rate through the inner torus are highly time variable. In animations of the funnel wall jet, increases in jet flux appear to be correlated with changes in the inner torus, suggesting that a build up of the inner torus can be one way to increase the mass flux through the jet.

3.3. The injection region

The injection region is where mass is transferred into the unbound outflow. Figure 4 shows the mass distribution as a function of radius in the jet, $M_{jet}(r) = \{\rho U^r\}_{jet}$, for all four KD models. These curves show two features: a region of relatively steep slope near the black hole, and a more extended region of shallow slope at larger radii. This extended region shows that mass entrainment takes place along the jet/corona boundary (if all matter injection were taking place near the base, this portion of the curve would be flat). The region of steep slope at small radii indicates that rapid matter injection occurs near the base of the jet. The point where mass injection begins moves inward with increasing black hole spin. The slope of the curve also steepens with increasing black hole spin. Apparently mass-loading of the jet can be enhanced by effects due to black hole spin.

In Paper I we noted that the mass flux in the jet increases outward along the radial extent of the inner torus, implying that the jet material found near the inner torus originates in it. The specific angular momentum, l , provides one marker to indicate the origin of the jet material, and near the black hole the specific angular momentum in the jet is comparable to the specific angular momentum in the adjacent inner torus at the same radius. Of course the centrifugal barrier ensures that l undergoes a sharp poleward transition through this region; high- l material is not found in the funnel. The thin layer of corona between the inner torus and the injection region contains elevated poleward mass flux (ρU^θ), also suggesting that

matter is moving from the inner torus to the corona, and hence to the jet. This poleward mass flux cuts off abruptly at the coronal interface to the jet, exactly where the region of strong outward radial mass flux begins.

What forces are responsible for injecting mass into the jet near the inner torus? Figure 6 shows vector plots of the poloidal components of the Lorentz and pressure-gradient forces [eqns. (5) and (6)]. The plot region is the same as that of Figure 5, and the circle indicates the location of the base of the jet. The arrows in the vector plots are scaled to the local zone dimensions and oriented along the local field direction. The color of the arrows is set by the magnitude of the force (in code units), and can be read on the color scale. The $-h U_t = 1$ contour, delineating the unbound flow, is shown as a thick white line. In addition, the azimuthally-averaged contours of density in the inner torus have been added in grey-scale.

This figure shows that in the inner torus and adjacent corona, the orientation of the poloidal force component is largely perpendicular to isodensity contours, consistent with pressure-supported hydrostatic equilibrium. In this figure the magnitude of the poloidal components of the gas pressure-gradient and Lorentz force are comparable, but since the inner torus and the thin corona surrounding it are highly dynamical, this is not always true. At other times there are regions within the corona where one or the other force components is dominant (see, e.g., fig. 8, Paper I which shows β in the disk and surrounding corona). Beyond the base of the jet, the net poloidal force is radially outward, with the outward-directed Lorentz force dominating the inward-directed gas pressure gradient. As noted earlier, the Lorentz force as shown here combines contributions from magnetic pressure gradients and stress terms. In the inner torus, it is the magnetic pressure gradient that contributes most to the Lorentz force; in the injection region and jet body, it is the stress contribution that is significant.

Figure 7 shows the azimuthally-averaged *toroidal* component of the Lorentz force near the base of the jet for model KDP. The plot region is the same as that of Figure 6, as is the color scale for the magnitude of the force component. This component of the Lorentz force corresponds to the familiar $B_r \nabla_r B_\phi$ Maxwell stress in nonrelativistic MHD; the toroidal gas and magnetic pressure gradients are negligible. The strength of the Maxwell stress is correlated with the spin of the black hole: it is weakest in model KD0, and strongest in model KDE. The Maxwell stress is prominent through the base of the jet, and passes through the base of the jet to the funnel side of the of the jet in the injection region and the jet body beyond. This pattern is seen in all models, and is indicative of magneto-centrifugal launching of the jet.

3.4. The funnel outflow

The general properties of the funnel outflow were discussed in Paper I, and its magnetic field in Paper II. Hydrostatic equilibrium is not possible within the funnel: material with significant specific angular momentum cannot get into the funnel, and any low- l material must either accrete into the hole, or leave as an outflow. Hence, the funnel remains largely evacuated throughout the simulations for all models; indeed, the density in the funnel approaches the floor value in some locations, particularly at large radius. Outflow velocities in the funnel are high, with radial values in the range $V^r \simeq 0.8\text{--}0.95$; these numbers should be regarded as qualitative indicators only.

In the present context, the most important aspect of the funnel is the presence of a large-scale organized poloidal magnetic field. Paper II showed that the funnel field has a radial structure similar to a split-monopole. This field is created as a result of wholesale field expansion: some of the closed fieldlines initially contained within the dense accretion flow near the equator slip outward into the region of very low mass density when the mass initially attached to them drains into the black hole. As they do so, they expand outward, creating the large-scale poloidal field that occupies the axial funnel. If the black hole is rotating, the funnel field is wound up and the toroidal field is amplified by frame dragging. Once the field in the funnel becomes comparable in magnitude to the adjacent field in the corona, its strength saturates and little further flux is drawn into the funnel.

As Figure 3 shows, the funnel outflow is a region of elevated outward energy flux but extremely weak mass flux. Although the density in the funnel outflow is very low, it has high internal energy. Compressive modes in the disk’s turbulence become nonlinear as they move down the steep density gradient at the edge of the funnel. Entropy is created in the resulting shocks, and the very low-density material in the funnel interior rises to very high temperature as a consequence. This leads to an enthalpy-dominated fluid energy flux. The electromagnetic energy flux increases with black hole spin as toroidal field is generated by frame-dragging.

3.5. The outflow region

In Paper I we noted an increase in the prominence of the jet’s radial mass flux, in relation to typical values in the main disk body, with increased black hole spin (e.g., fig. 10, Paper I). To put this on a more quantitative footing, we will examine the ejection rates of mass, energy, and angular momentum for unbound and bound material in the outflow region, taken to be just inside the outer radial boundary of the computational domain. The

fluxes are computed from the periodic full data sets which allow the values for bound and unbound flows to be distinguished.

Figure 8 shows a time-history of the ejection rates for mass, energy, and angular momentum for model KDP over the full 10 orbits of the simulation; the other KD models are similar. The solid curves show the total ejection rate, which contains contributions from the funnel outflow, the jets, and the bound coronal outflow. The specific value for the bound outflow is, of course, dependent on the location of outer grid boundary. The dashed lines show the ejection rates for the unbound portion flow which, because it is unbound, is expected to be largely independent of the location of the outer boundary.

Between times $t \approx 1.0 T_{orb}$ and $3.5 T_{orb}$ there are a weak and then a strong peak in the flux. The first peak is almost entirely made up of unbound material blown off the initial torus as the evolution begins; it reaches the outer boundary at about 1.5 orbits of time. The second, larger flux peak is made up of both bound and unbound material associated with the initial accretion into the black hole. As a thin equatorial stream of matter nears the black hole some material splashes back. Part of this outflow propagates along the funnel-wall, a precursor to the more permanent jet, and part of it comes from a bound outflow that moves along the surface of the disk (this surface outflow was noted in the SF models of DH03b). This mix of bound and unbound material takes about one orbital period after accretion begins to reach the outer boundary, giving rise to the second spike (this corresponds to a non-relativistic velocity $v \sim r_{max}/T_{orb} = 120 M/800 M \sim 0.15 c$). As the accretion flow becomes more fully established, the outflowing corona begins to contribute to the bound ejection rate. The jet emerges as a stable structure, with a continuous ejection of unbound material. The ejection rate remains somewhat variable, on a time scale comparable to the orbital period of the main disk, in contrast to the rapid variability of the accretion rate into the black hole (fig. 14 of Paper I). After the initial transients the unbound ejection rates have a mean value that is $\sim 10^{-6}$ of the initial mass/energy/angular momentum of the torus per unit time M for all models. This rate can be compared to the mean accretion rate into the black hole as reported in Paper I; these range from 1.78×10^{-5} for KD0, decreasing to 4.3×10^{-6} for KDE.

Table 1 lists the ejection rates for mass, energy, and angular momentum, computed using equation (2). The integrals were taken over the full simulation for each model in order to provide a consistent basis for comparison. The table lists the KD models, as well as other models that will be discussed in §4. For each quantity (Q), five columns are shown: the initial value, Q_0 ; the accretion rate of bound material through the inner boundary, ΔQ_i ; the bound (coronal) ejection rate, ΔQ_b ; the unbound (jet and funnel outflow) ejection rate, ΔQ_u ; and finally, the efficiency, $\eta_Q = \Delta Q_u/\Delta Q_i$, expressed as a percentage. For the KD models,

the ratio of unbound ejection to accretion increases with increasing spin, as can be seen by comparing ΔQ_u to ΔQ_i . The unbound mass flux normalized to the initial mass increases with black hole spin by a factor of 10 from KD0 to KDE. There is a similar increase in both the energy and angular momentum fluxes in the jets relative to the accreted quantities as a function of black hole spin. This suggests that the black hole spin itself may be a source of energy for the jets.

The efficiency measure, η_Q , compares ejection through the unbound outflow to accretion onto the black hole. The data in Table 1 shows a spin-dependent increase in this value for mass, energy, and angular momentum. Furthermore, there is a substantial jump in efficiency between models KDP ($a = 0.9$) and KDE ($a = 0.998$), especially for angular momentum. This jump is a clear manifestation of the non-linear contribution of black hole spin to the dynamics, and a demonstration that near-extreme Kerr holes can generate highly efficient jets.

In the KD simulations the initial torus serves as the mass source for the accretion flow. The transport of angular momentum allows accretion to occur, forming an accretion disk that extends down to near the black hole, where an inner torus forms near $1.5r_{ms}$. In following the mass flow through this system there are four quantities of interest: the bound flux through the radial shell at $r = 15.0 M$ (the inner edge of the initial torus), the amount of bound mass accreted into the black hole, and the amount of unbound mass carried off by the jets. What remains after accounting for these fluxes should be equal to the mass contained in the region inside $15M$ at the end of the simulation. Table 2 provides the numbers computed from the data dumps, and expressed as fractions of the initial torus mass for each model. The bound mass accreted into the black hole (ΔM_{hole}) and unbound mass carried off by the jets (ΔM_{jet}) are taken from Table 1. The flux of bound matter in the main disk and corona through the shell at $r = 15.0 M$ ($\Delta M_{r=15}$), is computed using the mass flux integral, $\langle \rho U^r \rangle_t(r = 15.0)$ with the condition $-h U^t < 1$. The final mass is computed at the end of the simulation by direct integration of the gas density inside $r = 15.0 M$. M_{final} should equal the amount that passed through $r = 15M$ minus the losses to the hole and in the jet. The agreement in these numbers is good, but not perfect. Two sources of error in this comparison are the possible entrainment of mass into the jet outside of $r = 15M$ in all models, and the need to evaluate the mass fluxes using the data dumps which are spaced at intervals of $80M$. One conclusion, however, is that unbound mass flux in the jets is a significant component of the mass flow through the near hole region for high-spin holes. The accretion flow at $r = 15M$ is mainly established by the MHD turbulence in the main body of the disk. The accretion rate into the hole, and, to some degree, the outflow rate in the jets are determined by processes near the black hole, and those rates need not match the accretion rate supplied by the main disk. One consequence is the spin-dependent build-up of the inner torus as noted in Paper I.

4. Jets in other simulations

In the preceding section we examined the unbound outflows that arise in the KD simulations. Jets have been seen in other accretion simulations as well. The present results raise several interesting questions that can be studied further by an examination of jets in those other simulations.

4.1. Jets in the SF simulations

The SF models (DH03b) consist of initial constant- l tori containing weak poloidal field loops. Three black hole spin values were considered: zero spin (SF0), prograde $a/M = 0.9$ (SFP), and retrograde $a/M = -0.998$ (SFR). The main difference between the SF and KD models is that the initial torus is hotter in the SF models, and the SFR model represents an example of a counter-rotating black hole. We find that jets are produced in all three SF models, including the extreme retrograde model SFR. This is noteworthy since the marginally stable orbit, at $r = 9M$, is quite distant from the black hole, and one might expect that the thin, elongated plunging inflow would not be conducive to jet formation. The base of the jet in the SFR model occurs just outside the static limit, i.e., well inside the marginally stable orbit. Despite this contrast, a jet is still produced in the retrograde case, although it is considerably weakened compared to the prograde models. The funnel wall is more flared out in SFR than in the prograde simulations, and consequently the jet has a relatively large opening angle near its base.

Table 1 presents information on the ejection rates for the SF models. It was noted in DH03b that these disk models generate rapid accretion, a fact that is reflected in the elevated rates shown in the table, e.g. 34% of the initial torus mass is accreted for model SF0, whereas only 16% is for model KD0. The greater accretion rate in the SF models is most likely connected to their greater heat content and therefore greater thickness. To the extent that magnetic stresses grow as longer-wavelength magneto-rotational modes become unstable, greater disk thickness promotes faster accretion. The ejection rates in the SF models are also elevated. This could arise from at least two possible causes: the greater rate at which mass is fed into the inner regions of the accretion flow, making it available to be expelled in the jet, and the greater amount of energy released by accretion, some of which can be utilized for driving outflows. One can regard energy drawn from the rotation of the black hole as catalyzed by accretion, so that the rate of rotational energy extraction, too, is proportional to the accretion rate.

4.2. Jets in pseudo-Newtonian simulations

There have been several investigations of black hole accretion in the pseudo-Newtonian approximation (Hawley & Krolik 2001, 2002; HB02; Kato *et al.* 2004). The initially poloidal simulation of Hawley & Krolik (2002) is very close in character to the KD0 model because it began from a hydrostatic initial condition with pressure maximum at $r = 20M$ and a purely poloidal magnetic field, and the pseudo-Newtonian potential was designed to mimic the principal properties of the Schwarzschild metric. HB02 was similar in design, but differed in that the initial condition was a constant angular momentum torus centered at $r = 200M$. The work of Kato *et al.* (2004) was similar to that of HB02, but for two different initial field strengths, and non-zero initial external gas pressure surrounding the accretion disk. Like HB02, the accreting matter was centered at relatively large distance, in this case $80M$.

In Hawley & Krolik (2002), although a high-temperature and (sometimes) magnetically dominated region is formed within a conical region near the axis, no true outflow is created; all the matter remains bound. By contrast, in HB02 a structure similar to that of KD0 was seen, a narrow outflow of unbound gas moving outward along the boundary between the corona and the funnel. At fixed height above the equatorial plane, the density is roughly constant in the corona, but then drops rapidly toward the axis. Gas pressure also drops through the jet body, but levels off in the funnel. In the corona, magnetic pressure dominates, but, unlike the KD models, the magnetic field in the funnel is not strong and β remains greater than 1. The field strength in the funnel has likely been reduced by the axial boundary condition, but this seems to have had little overall effect on the flow, which resembles what is seen in KD0. The primary jet acceleration mechanism in the HB02 model is the high gas pressure found near the centrifugal barrier. Jet collimation is due to the magnetized corona surrounding the jet. Kato *et al.* (2004) find a magnetic field configuration similar to the one reported in Paper II for the Schwarzschild hole simulation: radial field in the funnel surrounded by predominantly toroidal field. The jet that develops is driven by strong toroidal field pressures, and propagates in a $\beta \sim 1$ environment. The jet is collimated in large part by pressure from the surrounding corona.

Although pseudo-Newtonian dynamics can, in many respects, be a good approximation to the dynamics in a Schwarzschild metric, the effects of black hole rotation cannot be reproduced in this way. The dramatic strengthening of the outflow with increasing a/M is an intrinsically relativistic effect.

4.3. $\Gamma = 4/3$ equation of state

Since gas pressure acceleration plays a role in the acceleration of the jet, it is of interest to see how the jet might vary with the adiabatic index, Γ . Model KDPi is similar to KDP except that it employs the softer $\Gamma = 4/3$ equation of state. From Table 1 we see that this model yields a slightly weaker jet than the corresponding $\Gamma = 5/3$ simulation; only 0.21% of the initial torus mass is ejected in the jet, compared to 0.30% for KDP. A similar reduction occurs for energy and angular momentum. However, the accretion rates are similarly affected, resulting in comparable efficiencies for models KDP and KDPi. Any dependence of the jet on the equation of state in this simulation seems to be modest.

4.4. Initial toroidal field

In this simulation, the Schwarzschild (KD0) torus is initialized with a moderate ($\beta = 10$) *toroidal* field. The grid resolution is $128 \times 128 \times 64$. This model eventually generates an accretion flow produced by MRI-driven turbulence. What is notable for the present purposes is that this model generates essentially no jet.

Several factors may all contribute to suppressing the jet. The accretion rate is considerably weaker in this simulation, and the flow does not form a substantial inner torus, so there is no large pressure gradient to push material against the funnel wall. But, perhaps more importantly, there is no significant poloidal magnetic field in the funnel. In the KD models, an extended poloidal field is generated by the plunging accretion flow, and this field is ejected into the funnel when that flow reaches the black hole. This becomes the radial funnel field, whose polarity is established by the initial conditions. In the toroidal field model, there is no initial north/south field mirror symmetry, and no large-scale, systematic poloidal field lines generated by the inflow. Thus the toroidal field model provides an example of jet formation switched off, while illustrating that radial funnel fields need not be the inevitable consequence of accretion.

4.5. Numerical resolution

The values shown in Table 1 for low-resolution model KDPlr are comparable to those of model KDP. The amount of material ejected through the jet is very similar for mass, energy, and angular momentum. However, the corresponding accreted quantities are systematically lower, yielding slightly higher efficiencies for model KDPlr. As noted in Paper I, the increased numerical resolution in the “high resolution” KD models better captures the turbulent and

highly dynamical accretion flow. However, the constancy of the ejected rates between the two models suggests that the present numerical resolution is adequate to capture the qualitative behavior of the jets.

4.6. Axisymmetric Simulations

To the extent that our results reflect physical processes likely to occur in accretion systems, they should be reproducible and seen in other global models. Although global simulations of this type are still uncommon, jets similar to what we report here have been observed by McKinney & Gammie (2004) who have carried axisymmetric GRMHD simulations of a torus around an $a/M = 0.938$ black hole. They find the same general late-time flow structures as characterized in Paper I, including a conical mass outflow along the funnel edge, along with a significant electromagnetic flux in the funnel. The unbound material in this outflow begins just inside the equipartition contour $\beta = 1$. The funnel is evacuated and contains a large-scale radial field. Because their simulations make use of a quite distinct numerical algorithm, and greater (albeit two-dimensional) grid resolution, the overall agreement of the results is gratifying.

5. Conclusion

Unbound outflows are a natural outcome of accretion in our self-consistent MHD disk simulations. They carry a non-negligible flux of energy and momentum, and are collimated and confined to the axial funnel. These outflows are distinct from the coronal outflows which remain bound. There are two components to the unbound outflows: a hot, fast, and tenuous outflow through the axial funnel and a colder, slower, massive jet confined to the funnel wall by the centrifugal barrier. We observe jets in a wide range of simulations, for both rotating and nonrotating black holes. While the jets appear in quite general conditions, their strength is determined by the accretion rate, the pressure in the inner torus, and the spin of the black hole, factors which are themselves interdependent. The funnel outflows have a strong spin-dependent growth in energy flux, which is their distinguishing characteristic.

Both gas pressure gradients and Lorentz forces in the inner torus seem to play a significant role in launching the jets. The base of the jet is located at a point close to the black hole where the inner torus, corona, and funnel meet. Mass is injected into an unbound outflow and that is driven by magneto-centrifugal acceleration due to the disk rotation. This mechanism can operate even around Schwarzschild black holes, although the jets produced

are relatively weak. Strong gas pressure gradients can also play a role. These gradients are the predominant acceleration mechanism in the pseudo-Newtonian model of HB02, and funnel-wall jets can even occur in purely hydrodynamic black hole accretion flows if the inflowing gas is hot enough and there is pressure confinement in the coronal region (Hawley 1986).

The KD models develop a large-scale poloidal, mainly radial, magnetic field in the funnel which comes from magnetic field injected into the funnel when the accretion flow first reaches the black hole. The resulting field is in pressure balance with the surrounding corona. The poloidal field lines extend into the ergosphere and this permits frame dragging to tap into the rotational energy of the black hole, increasing the flux of energy in the funnel outflow and the funnel-wall jet in the models with a spinning black hole. Although this mechanism is reminiscent of the scenario proposed by Blandford & Znajek (1977) in that energy is extracted by the magnetic field from a rotating hole, the role of matter is much more important here than in the original Blandford-Znajek picture. Much of the energy flux in the funnel outflow and funnel-wall jet comes from the fluid enthalpy, not just the electromagnetic component. In addition, in the classical Blandford-Znajek picture, the density was so low everywhere that the field was taken to be “force-free”; here, by contrast, most of the mass and energy flow occur in the funnel-wall jet, where the ratio of magnetic field energy density to matter energy density is generally less than unity.

In the SF simulations jets are generated by both prograde and retrograde accretion flows, although the jets are considerably weaker in the latter case. The elevated accretion rates of the SF models are accompanied by higher ejection rates; the thicker and hotter inner tori in these models may be part of the cause. We see only a weak dependence on the equation of state, but the role of the vertical thickness and temperature of the inner torus in jet formation is a topic requiring further study. Pseudo-Newtonian simulations can also generate jets comparable in strength to those observed in Schwarzschild simulations. The apparent differences in jet strength and driving mechanisms between the various pseudo-Newtonian simulations raise several questions for further study. Together, these simulations provide support for the idea that unbound outflows are a natural outcome of accretion. However, it is possible to switch off jet production if the accretion rate into the inner region of the computational volume is significantly reduced, or when there is no significant poloidal field in the funnel, as was the case when an initially toroidal magnetic field configuration was used.

In regards to more general issues, our results certainly support the position that MHD is essential for jet formation and collimation. The prospects for purely hydrodynamic processes do not look promising. While gas pressure alone can accelerate gas away from a sufficiently

hot inner torus, any angular momentum that gas has will keep it out of the funnel, and collimation can occur only if there is a substantial corona providing confining pressure. Even in the pseudo-Newtonian simulation of HB02, where the jet acceleration is pressure driven and funnel fields are not important, the confining corona is magnetically dominated.

But do jets require an initial net large-scale poloidal field? While such fields clearly can produce substantial jets, they are not essential. The jets produced in these simulations developed from initial conditions in which the magnetic field was completely contained within a gas torus. Most of the field subsequently generated by the accretion disk is toroidal, and this field fills the corona and helps to collimate the jet. The large-scale poloidal field that forms is confined mainly to the funnel, and its strength is limited to equipartition with the surrounding coronal pressure. However, even this modest field can have a quantitative effect on the jet as it facilitates the extraction of spin energy from the hole.

Finally there is the question of what specific physical mechanism produces jets. Here we can give no simple answer. Strong pressure gradients, both magnetic and hydrodynamic, magnetic forces analogous to those considered by Blandford & Payne, and energy extraction from the rotating hole, as in the Blandford & Znajek scenario, all appear to play a role in different circumstances. To the extent that numerical simulations can provide a window on reality, it is emerging once again that while simplified theoretical models shed light on aspects of reality, “all of the above” seems to be the answer to the question of which mechanism is responsible for launching jets from an accretion flow.

The work of JFH and JPD was supported by NSF grant AST-0070979 and NSF ITR grant PHY02-05155. JHK and SH were partially supported by NSF grants AST-0205806 and AST-0313031 (JHK and SH). The simulations were carried out on the Bluehorizon system of NPACI. We thank Charles Gammie and Jonathan McKinney for the discussion of their results. JHK is also grateful to the Institute of Astronomy, Cambridge for its hospitality while this work was completed, and to the Raymond and Beverly Sackler Fund for support during his visit there.

REFERENCES

- Abramowicz, M. A., Jaroszyński, M., & Sikora, M. 1978, *A&A*, 63, 221.
- Balbus, S. A. & Hawley, J. F. 1998, *Rev. Mod. Phys.*, 70, 1
- Blandford, R. D. & Znajek, R. 1977, *MNRAS*, 179, 433

- Blandford, R. D. & Payne, D. 1982, MNRAS, 199, 833
- De Villiers, J. P. & Hawley, J. F. 2003, ApJ, 589, 458 (DH03a)
- De Villiers, J. P. & Hawley, J. F. 2003, ApJ, 592, 1060 (DH03b)
- De Villiers, J. P., Hawley, J. F., & Krolik, J. H. 2003, ApJ, 599, 1238 (Paper I)
- Hawley, J. F. 1986, in Radiation Hydrodynamics in Stars and Compact Objects, ed. D. Mihalas and K.-H. Winkler (New York: Springer-Verlag), 369
- Hawley, J. F., & Balbus, S. A. 2002, ApJ, 573, 738 (HB02)
- Hawley, J. F. & Krolik, J. H., 2001, ApJ, 548, 348
- Hawley, J. F. & Krolik, J. H., 2002, ApJ, 566, 164
- Hirose, S., Krolik, J. H., De Villiers, J. P., & Hawley, J. F. 2004, ApJ, 606, 1083 (Paper II)
- Kato, Y., Mineshige, S., & Shibata, K. 2004, ApJ, 605, 307
- Krasnopolsky, R., Li, Z.-Y., & Blandford, R. D. 1999, ApJ, 526, 631
- Livio, M. 2002, Nature, 417, 125
- McKinney, J. C., & Gammie, C. F. 2004, ApJ, in press
- Meier, D. L., Eddington, S. Godon, P., Payne, D. G., & Lind, K. R. 1997, Nature, 388, 350
- Misner, C. W., Thorne, K. S., & Wheeler, J. A 1973, Gravitation (San Francisco: W.H. Freeman)
- Ouyed, R., & Pudritz, R. E. 1997, ApJ, 484, 794
- Punsly, B., & Coroniti, F. V. 1990, ApJ, 354, 583
- Romanova, M. M., Ustyugova, G. V., Koldoba, A. V., Chechetkin, V. M., & Lovelace, R. V. 1997, ApJ, 482, 708
- Shibata, K. & Uchida, Y. 1985, PASJ, 37, 31

Table 1. Ejection from Outer Boundary

Model	M_0	ΔM_i	ΔM_b	ΔM_u	η_M	E_0	ΔE_i	ΔE_b	ΔE_u	η_E	L_0	ΔL_i	ΔL_b	ΔL_u	η
KD0	156	24.9	1.14	0.17	0.7	154	22.7	1.14	0.22	1.0	902	77.1	6.85	0.44	0
KDI	258	36.1	2.70	0.60	1.7	255	32.8	2.69	0.94	2.9	1489	95.0	17.2	3.02	3
KDP	291	17.9	1.86	0.87	4.8	286	15.0	1.85	1.63	11	1652	33.5	9.12	4.10	0
KDE	392	14.4	8.35	4.78	33	386	9.34	8.33	9.67	104	2255	14.1	55.2	23.0	1
KDPi	151	5.73	0.48	0.32	5.6	148	4.79	0.47	0.54	11	835	10.8	2.34	1.52	0
KDPI	291	10.2	0.88	0.87	8.5	286	8.33	0.88	1.52	18	1652	19.2	4.21	3.68	0
SFR	741	285	8.76	1.36	0.5	726	272	8.73	1.67	0.6	3484	1102	46.0	2.19	0
SF0	1374	469	24.6	6.78	1.4	1346	441	24.5	6.88	1.6	6058	1455	113	24.7	1
SFP	2308	427	72.3	30.2	7.1	2263	369	72.1	38.4	10	9729	759	289	116	0

Table 2. Mass flux in the inner region

Model	ΔM_{hole}	ΔM_{jet}	$\Delta M_{r=15}$	M_{final}
KD0	0.161	0.00147	0.184	0.0194
KDI	0.141	0.00275	0.171	0.0259
KDP	0.062	0.00361	0.101	0.0281
KDE	0.038	0.01400	0.115	0.0545

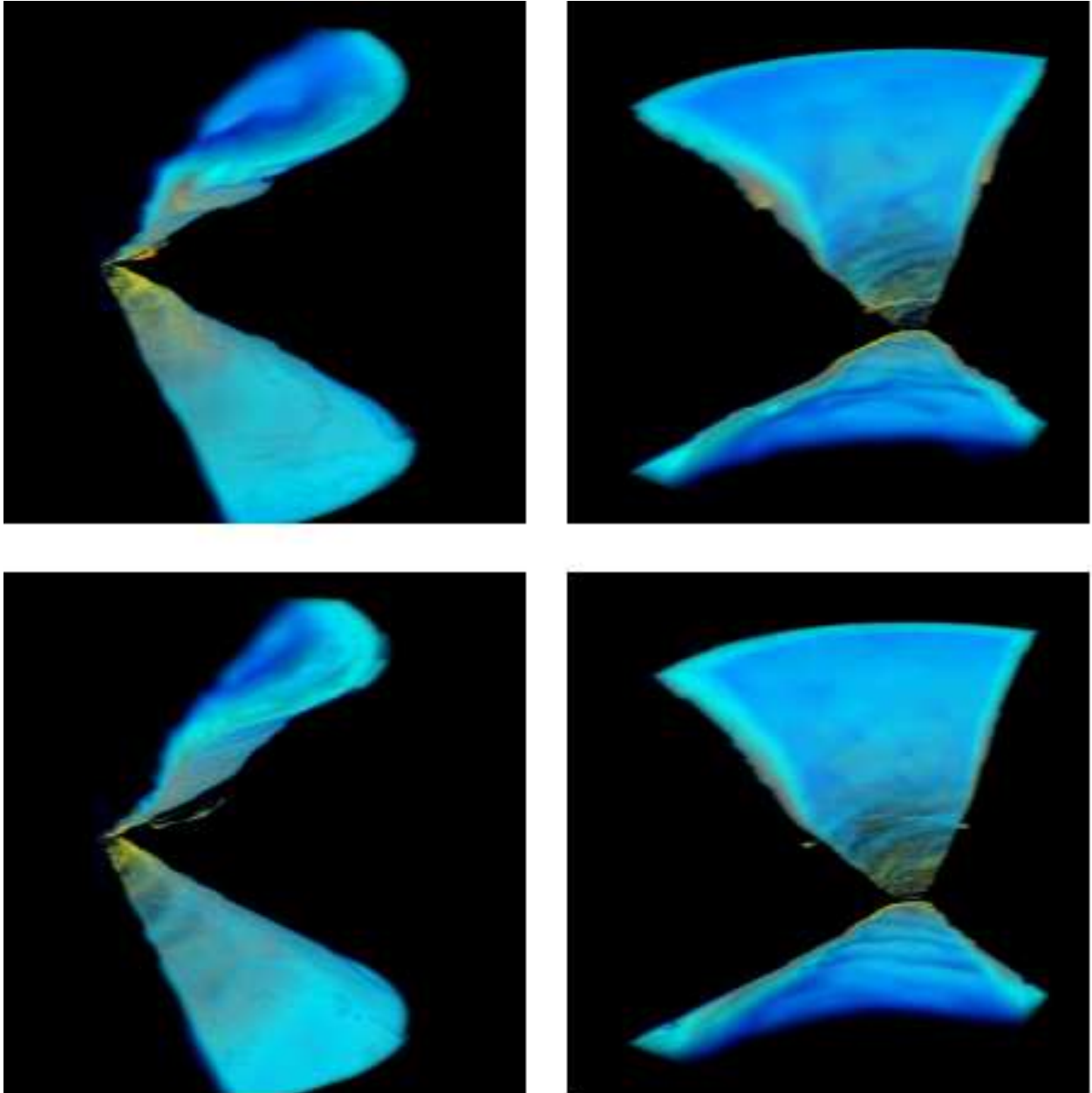


Fig. 1.— Still frames taken from an animation of the density ρ in the jets for model KDP, i.e., where $U^r > 0$ and $-hU^t > 1$. The top row shows two views of the jet at $t = 7840 M$; the bottom row is for $t = 8080 M$. One view looks outward from the polar axis, the other inward from outside the jet. The shape corresponds to the quarter-plane ϕ coordinate range used in the simulation. The outer boundary of the image is at $r \approx 60 M$. The density is plotted as a volumetric rendering using a logarithmic scale, where blues indicate densities in the range of 10^{-4} to 10^{-3} , grey values near 10^{-2} , and yellows and reds values in the range 10^{-1} to 10^0 relative to a fiducial value taken at the base of the jet.

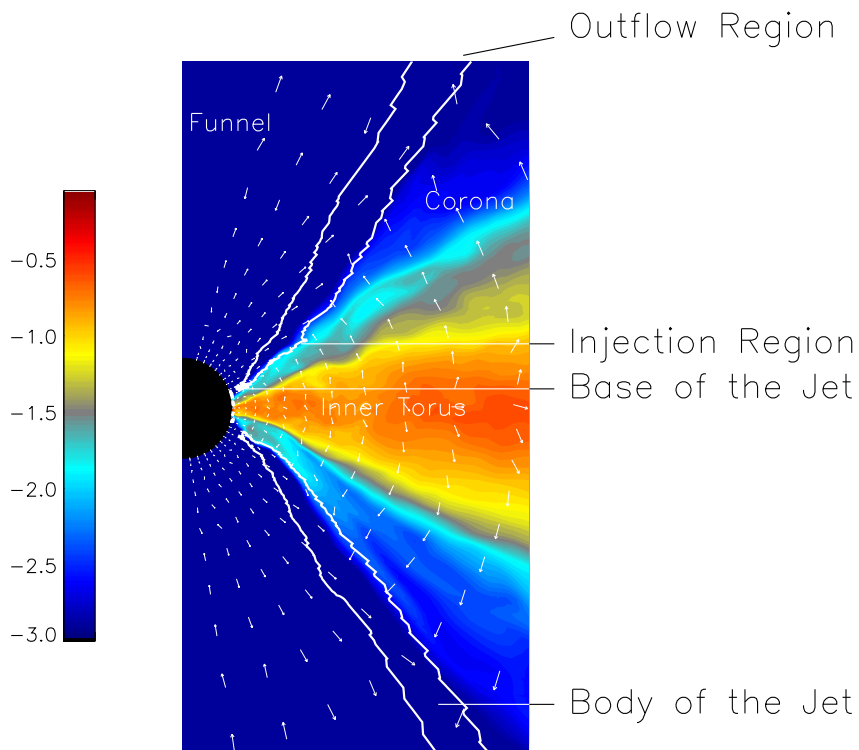


Fig. 2.— General structural features of the jets. This plot shows a composite view of several azimuthally-averaged late-time quantities for model KDP. In general, the jet is well-established after two orbital periods of the main disk, and the features shown here apply equally to all models that exhibit jets. The color contours show gas density (ρ) on a logarithmic scale. The boundary of the jet is indicated by a thick white contour (see text for explanation). The vector field indicates the direction, but not the magnitude of the net forces acting on the accretion system. The length of the arrows is scaled to the local zone width. Not all vectors are shown; a stride of 8 was used in both the radial and polar grids to reduce the density of the vector plot.

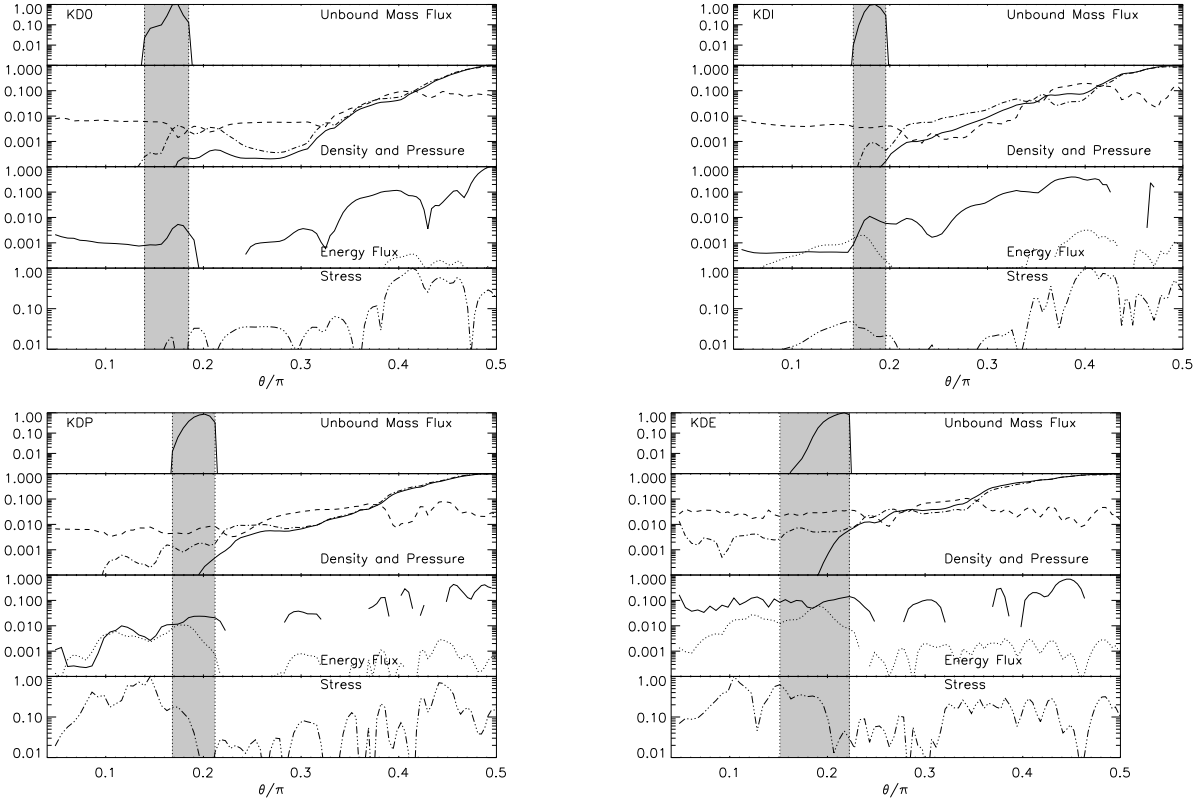


Fig. 3.— Cross-section of key code variables through the body of the jet taken from the late-time simulation data ($t = 8080 M$) for the four KD models. Each plot shows azimuthally-averaged quantities plotted as functions of polar angle θ . For consistency across models, the cross-sections are taken at a radial distance of $10 r_{ms}$. The top graphs in each panel show mass flux, ρU^r , which defines the jet boundaries. The second row of graphs show density (solid line) as well as gas (dash-dot line) and magnetic pressure (dashed line). The third row of graphs shows the fluid (solid line) and electromagnetic (dashed line) components of outward energy flux (gaps in the curves correspond to radially inward flux). The bottom graphs show the absolute value of the magnetic stress.

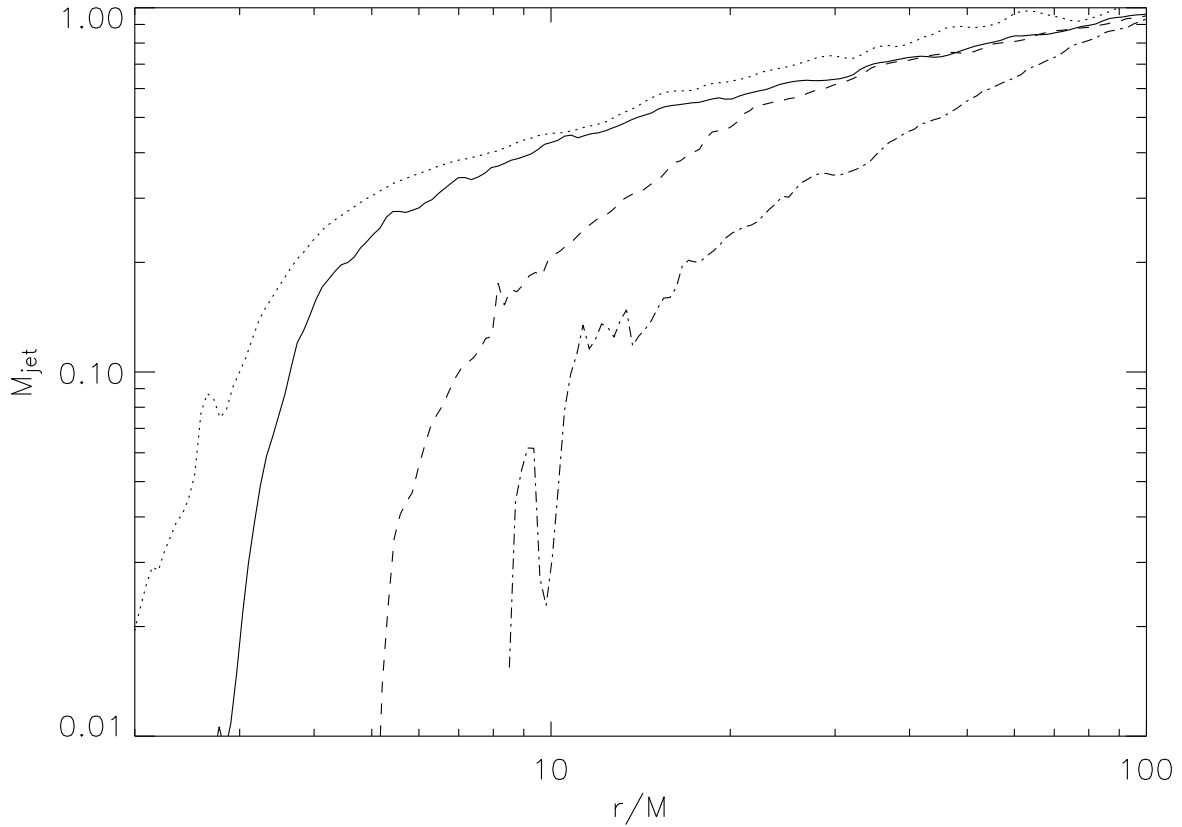


Fig. 4.— Mass distribution in the jet, $M_{jet}(r) = \{\rho U^r\}_{jet}$, for model KDP (solid line), KD0 (dash-dot line), KDI (dashed line) and KDE (dotted line). Each curve is normalized to the maximum, which occurs at the outer radial boundary. The shallow slope at large radii indicates that mass entrainment is taking place in this region for all models. The steep slope at small radii indicates the rapid injection of mass into the jet over a small radial distance. This injection region is mostly missing in model KD0, and strongest in the high-spin models KDP and KDE.

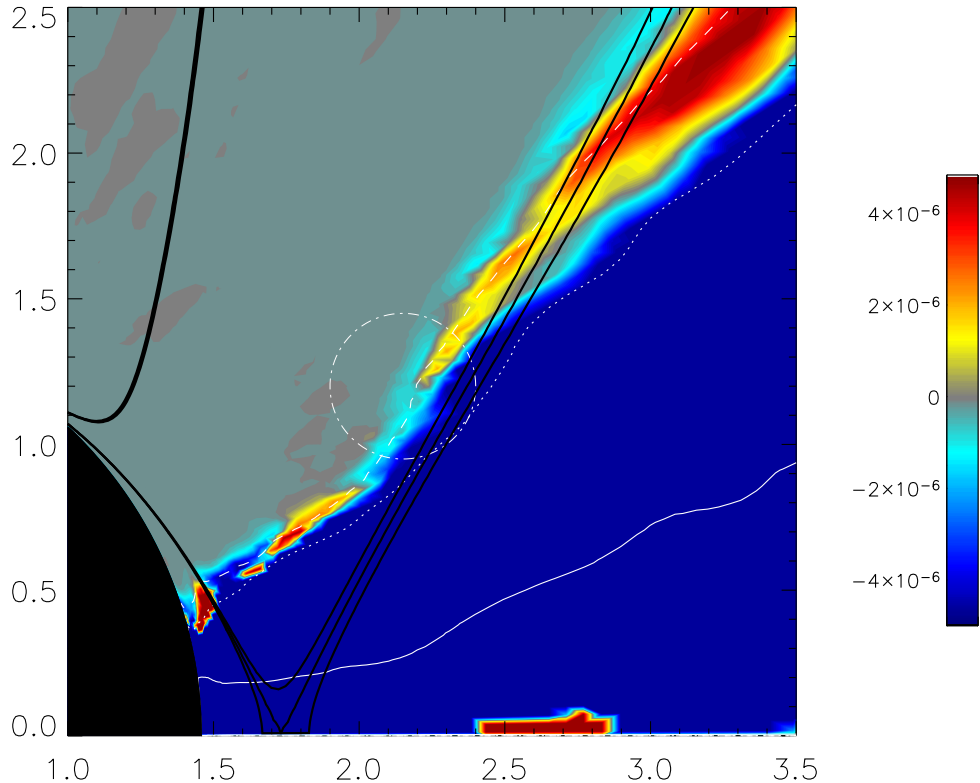


Fig. 5.— The azimuthally-averaged radial mass flux, $\langle \rho U^r \rangle_\phi$, near the base of the jet for model KDP (at $t = 8080 M$), above the equatorial plane. Three density contours have been added to locate the disk, $10^{-3} \rho_{max}$ (dashed line), $10^{-2} \rho_{max}$ (dotted line), $10^{-1} \rho_{max}$ (solid line). The base, highlighted by a circle, features both an outgoing and ingoing component. The extended region of outbound material outside the 10^{-3} density contour is unbound (this density contour approximately follows the funnel wall in this region of the flow). Equipotentials for marginally bound gas (see text for details) are also shown as thick black lines; the contours bracket the critical contour, $\Phi_{mb} = [-0.01, 0, 0.01]$.

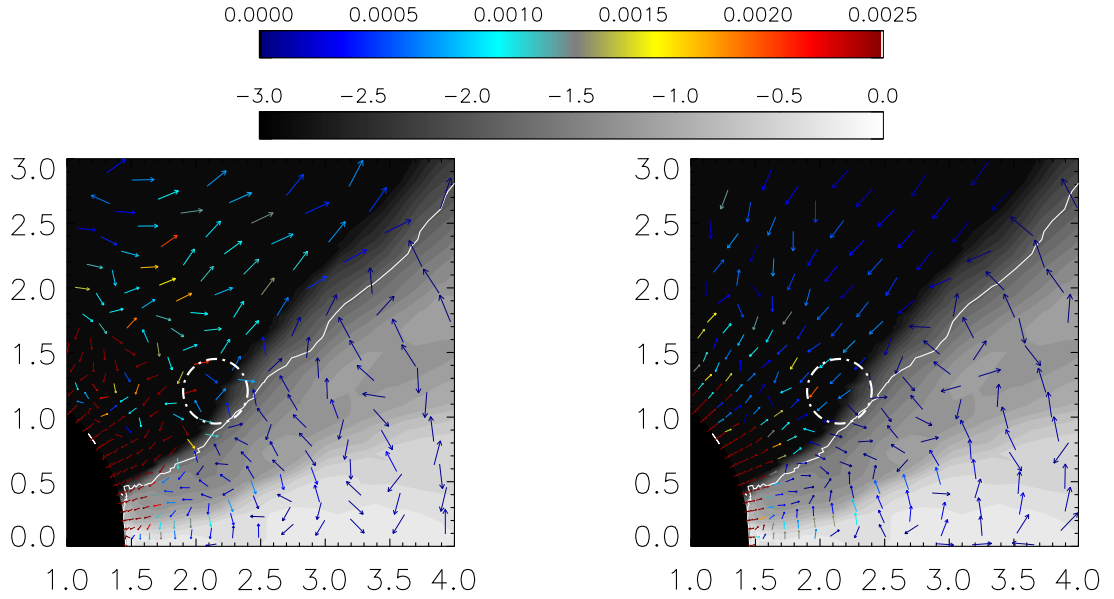


Fig. 6.— The azimuthally-averaged poloidal components of the Lorentz force (left panel) and pressure gradient (right panel) near the base of the jet, model KDP (at $t = 8080 M$). The vectors carry magnitude information in their color (see accompanying scale, in code units); the length of the vectors is proportional to the local zone width. For reference, azimuthally-averaged density contours are shown on grey-scale. The base of the jet is highlighted by a circle, and the solid white line marks the $-hU_t = 1$ contour, which marks the coronal boundary of the funnel-wall jet. Near the base, the Lorentz and pressure gradient contributions to the force are normal to the surface of the disk and divert matter from the inflow into the jet.

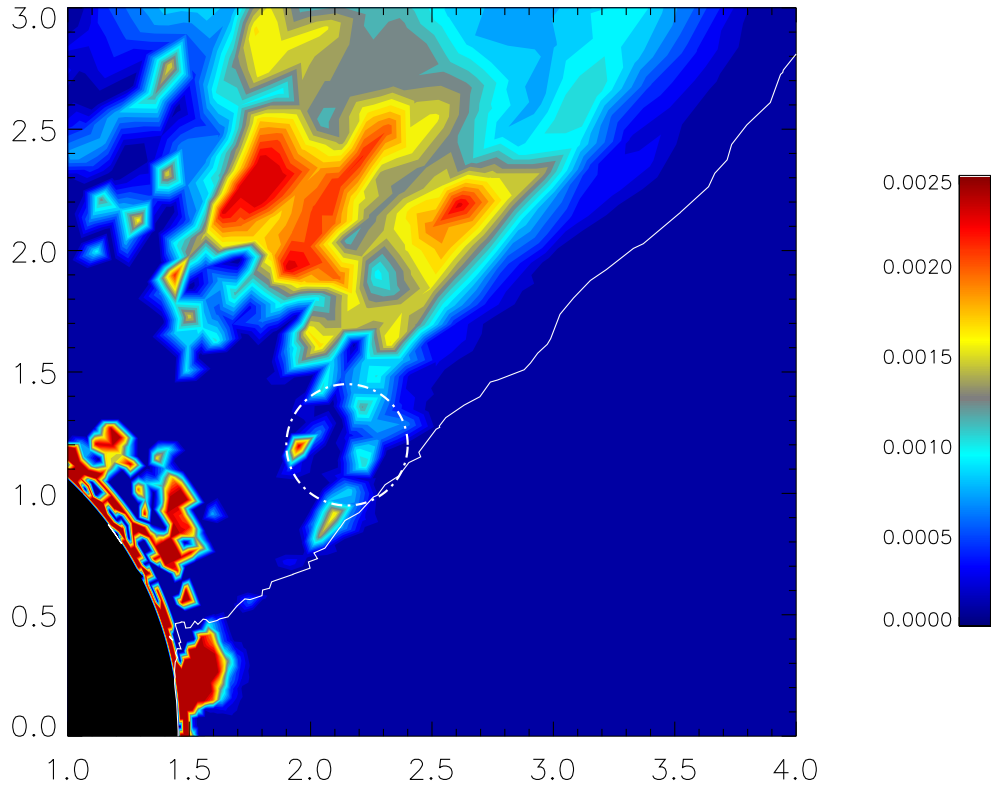


Fig. 7.— The azimuthally-averaged toroidal component of the Lorentz force near the base of the jet, model KDP (at $t = 8080 M$). The magnitude of the force is indicated in the accompanying color scale (in code units). The base of the jet is indicated by a circle, and the solid white line is the $-hU_t = 1$ contour, which marks the boundary of the unbound outflow. The Lorentz force shows a strong contribution both at the base of the jet, and on the funnel interface of the jet. A similar plot of the toroidal component of the pressure gradient (not shown) indicates that the Lorentz force is dominant in the funnel.

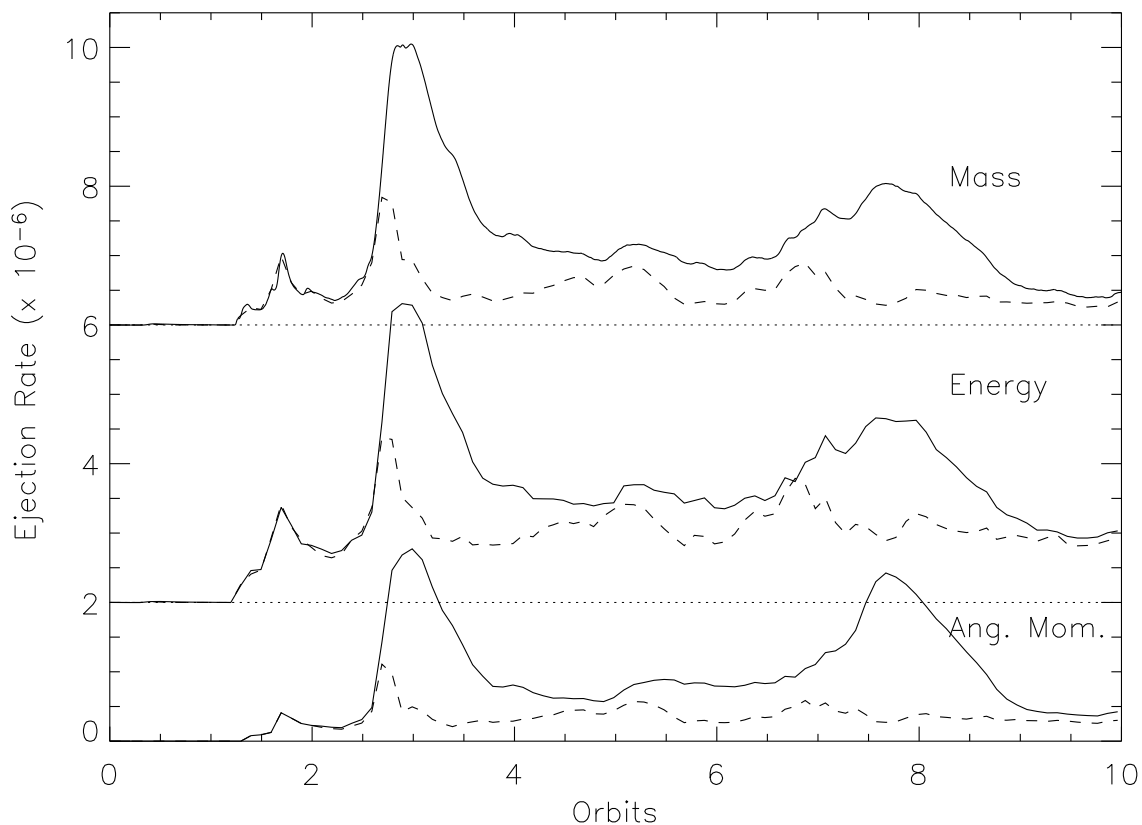


Fig. 8.— The ejection rate of mass, energy, and angular momentum through the outer radial boundary as a function of time for model KDP. The solid lines represent the rate for both bound and unbound matter; the dashed lines represent the unbound portion. The units are fraction of initial torus mass/energy/angular momentum accreted per unit time M . For clarity, the mass and energy curves are shifted vertically by 7.0 and 3.0×10^{-6} , respectively.